www.acsnano.org

# How Precisely Can Individual Molecules Be Analyzed? A Case Study on Locally Quantifying Forces and Energies Using Scanning Probe Microscopy

Xinzhe Wang, Percy Zahl, Hailiang Wang, Eric I. Altman, and Udo D. Schwarz\*



Downloaded via YALE UNIV on February 13, 2024 at 03:44:13 (UTC). See https://pubs.acs.org/sharingguidelines for options on how to legitimately share published articles.

Cite This: ACS Nano 2024, 18, 4495–4506



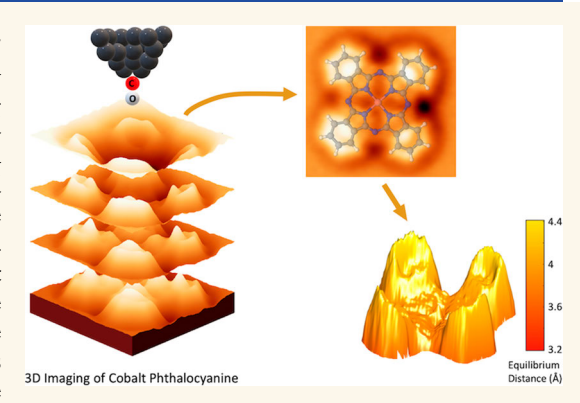
**ACCESS** 

Metrics & More

Article Recommendations

Supporting Information

ABSTRACT: Recent advances in scanning probe microscopy methodology have enabled the measurement of tip-sample interactions with picometer accuracy in all three spatial dimensions, thereby providing a detailed site-specific and distance-dependent picture of the related properties. This paper explores the degree of detail and accuracy that can be achieved in locally quantifying probe-molecule interaction forces and energies for adsorbed molecules. Toward this end, cobalt phthalocyanine (CoPc), a promising CO<sub>2</sub> reduction catalyst, was studied on Ag(111) as a model system using low-temperature, ultrahigh vacuum noncontact atomic force microscopy. Data were recorded as a function of distance from the surface, from which detailed three-dimensional maps of the molecule's interaction with the tip for normal and lateral forces as well as the tip-molecule interaction potential were constructed. The data were collected with a CO molecule at the tip apex, which enabled a detailed



visualization of the atomic structure. Determination of the tip—substrate interaction as a function of distance allowed isolation of the molecule—tip interactions; when analyzing these in terms of a Lennard—Jones-type potential, the atomically resolved equilibrium interaction energies between the CO tethered to the tip and the CoPc molecule could be recovered. Interaction energies peaked at less than 160 meV, indicating a physisorption interaction. As expected, the interaction was weakest at the aromatic hydrogens around the periphery of the molecule and strongest surrounding the metal center. The interaction, however, did not peak directly above the Co atom but rather in pockets surrounding it.

KEYWORDS: cobalt phthalocyanines, noncontact atomic force microscopy, scanning tunneling force microscopy, three-dimensional atomic force microscopy, site-specific quantification of forces, surface catalysis, molecular catalysts

# **INTRODUCTION**

Scanning probe microscopy (SPM) has emerged as a powerful tool in the field of nanoscale characterization, enabling not only "topographical" surface imaging but also precise and often distance-dependent measurements of a variety of tip—sample interactions. For chemical research, advancements in SPM methodology that allow the quantification of interaction forces and energies at the piconewton and millielectronvolt scale and with picometer spatial resolution are of particular importance, as such information provides valuable insights into a material's behavior. For example, understanding and controlling the interactions exhibited by molecules and/or between molecules is crucial for optimizing their performance in diverse applications such as surface chemistry, heterogeneous catalysis, thin-film growth, and even aspects of quantum

device research.<sup>25</sup> To facilitate such studies, we here provide a step-by-step roadmap toward complete high-resolution analysis of local force and energy interactions exhibited by molecular catalysts immobilized on surfaces. Issues specifically addressed include (i) what level of accuracy is achievable by combining advanced scanning probe microscopy-based data acquisition methods, postacquisition data processing, and tip functionalization; (ii) how to account for the effect of the substrate on the

Received: November 12, 2023 Revised: January 17, 2024 Accepted: January 18, 2024 Published: January 24, 2024





measured molecule—probe interaction; (iii) how close the probing tip can approach the molecule without altering the observed interactions by elastically deforming the molecule, the substrate, and/or the tip; and (iv) how, given such limitations, we can gain estimates for the interaction energies the immobilized molecule would locally exhibit toward potential reactants at equilibrium distances.

To illustrate the set of measurement protocols developed in this work, we employ cobalt phthalocyanine (CoPc) molecules adsorbed on a Ag(111) surface as a model system. Due to their large number of uses, phthalocyanines are frequently studied in contexts that range from thin-film devices such as solar cells to corrosion inhibitors to applications in medicine or catalysis. 26-32 For example, immobilized CoPc has recently garnered interest as a promising hybrid catalyst for methanol production from electrochemical  ${\rm CO_2}$  reduction.<sup>33–36</sup> In this application, the adsorption strength of carbon monoxide on the central cobalt atom has been identified as the descriptor for both activity and selectivity to methanol formation. Thus, optimizing this parameter is crucial: if adsorption is too weak, mostly CO is produced; conversely, too strong bonding causes the CO to irreversibly bind, effectively stopping methanol production altogether.<sup>33</sup> This goal motivates studying how CO interacts across individual CoPc molecules; the commonplace CO tip functionalization in SPM makes this goal accessible. 2,5,39-44

An advantage of working with a molecular catalyst, as opposed to conventional heterogeneous catalysts (e.g., copper for CO<sub>2</sub> to hydrocarbon fuels conversion<sup>45–48</sup>), is that for molecules there are numerous ways to finely and uniformly tune the center metal atom's binding strength. For CoPc, this can be achieved by (i) switching the substrate the CoPcs are deposited on; (ii) injecting or withdrawing electrons from the center Co through adding appropriate side chains to the Pc ligand; or (iii) changing the distance between the molecular catalyst and the substrate. Options to accomplish the latter include inducing moleculesubstrate bond formation, which pulls the molecule toward the substrate, or adding bulky side chains that lift the center of the molecule, thereby increasing the distance between the Co and the support and weakening the impact of the support. Future investigations are therefore aimed at applying the same measurement protocols to these modifications and then comparing the results. By doing so, the effects each change will cause on an intermolecular scale will be revealed, which is key for reaction optimization.

To collect the data, we employed a low-temperature, ultrahigh vacuum scanning probe microscope operated in noncontact atomic force microscopy (NC-AFM) mode. This approach, combined with postacquisition data analysis procedures, enabled the generation of detailed three-dimensional images of the molecule's interaction with the CO-terminated probe tip. To gain comprehensive insight into the system's properties, we investigate both normal and lateral forces as well as the tipsample interaction potential. Leveraging the piconewton and millielectron resolution provided by our method and adaptive interpolation methods, we construct a picometer-spaced threedimensional (3D) array of data points that allows seamless determination of the tip-substrate interaction as a function of distance; the procedure to obtain this array is referred to as 3D-AFM. 4,13-15 By subtracting the tip-substrate interaction from the data collected above the adsorbed molecule, we can isolate the CoPc-tip interactions (referred to later as the "target interactions"), which are then used as a stepping stone for extracting estimates for the equilibrium interaction energies

between the adsorbed CoPc and the carbon monoxide molecule on the tip. These equilibrium energies serve as vital indicators of the CoPc's local behavior; thanks to the termination of the tip with a CO molecule, they represent the best experimental sitespecific insight to date into the catalytic properties of individual CoPc molecules and potentially other similar systems. The results reveal a physisorption interaction of CoPc with the downward projecting O atom of the tethered CO molecule that maximizes in pockets surrounding the central Co atom. More generally, the picometer precision of locally measuring forces and energies at surfaces that can be achieved by combining advanced SPM techniques with sophisticated data analysis procedures not only contributes to the fundamental understanding of molecular interactions but also holds promise for enhancing the design and performance of materials in various scientific and technological domains.

# **RESULTS AND DISCUSSION**

Adsorption Configurations. Energy landscapes and force maps of molecules on a support are generally highly dependent not only on the nature of the support but also on the precise adsorption geometry. Different adsorption sites and geometries can result in variations of the molecule—substrate binding energy and charge transfer between the molecules and the substrate. Figure 1b showcases a "stitched-together" large-scale

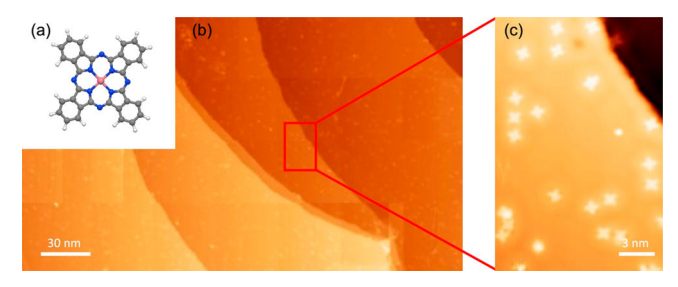


Figure 1. (a) Ball-and-stick model of a cobalt phthalocyanine molecule. Carbon atoms are gray, nitrogen is blue, hydrogen is white, and the center cobalt atom is pink. (b) Overview scanning tunneling microscopy image of Ag(111) with adsorbed CoPc molecules; this image has been stitched together by combining 12 individual images recorded with a resolution of  $800 \times 800$  pixels into one. Individual steps visible on the Ag(111) crystal are monatomic, i.e., 2.35 Å in height each. (c) Zoom into the area highlighted in (b) with the red rectangle. At this magnification, the cross-like shape of individual CoPc molecules is easily discernible.

scanning tunneling microscopy (STM) image that provides a representative overview of the spatial distribution and arrangement of CoPc molecules on the Ag(111) surface; the distinct cross-like shapes of individual CoPc molecules (Figure 1a) are then apparent when zooming in to somewhat higher resolution (Figure 1c).<sup>49</sup> Upon closer examination, standing charge waves surrounding individual CoPcs can be observed; <sup>50</sup> note that the (111) surfaces of group IB metals are well-known for exhibiting surface charge waves that align with either surface steps or surface point defects such as vacancies, impurities, or adsorbed atoms and molecules. <sup>50–53</sup>

In light of the above considerations, we started this study by investigating the adsorption behavior of individual CoPc molecules relative to the underlying silver's crystallographic axes in a statistically meaningful manner. Two examples of how this task was conducted are presented in Figure 2, where the inset provides a high-resolution STM image of the atomic

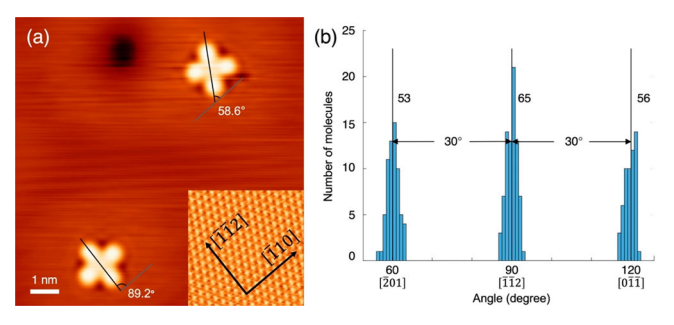


Figure 2. (a) STM image of two differently oriented CoPc molecules on Ag(111). Inset: atomic resolution STM image of the Ag(111) substrate. The scale and orientation in the inset were kept the same as the main figure. (b) Histogram of the orientation angle distribution of 174 different isolated CoPc molecules on Ag(111). The values of the orientation angles were measured with reference to the substrate's  $[\bar{1}10]$  direction as indicated in the inset of panel (a), and each blue bar covers 1° in width. The numbers displayed right of each peak represent the total number of molecules found within each individual peak.

structure of the Ag(111) substrate. The full sampling process involving analysis of 174 molecules resulted in the histogram in Figure 2b, where the angle between one axis of the cross-like shape of the CoPc molecules and the substrate's [110] direction is plotted on the histogram's horizontal axis. Three distinct orientations were found: 60°, 90°, and 120°, which indicates that one of the lobes of the crosses always aligns with a close-packed direction of the Ag(111) substrate. However, closer quantitative inspection reveals that the  $60^{\circ}$  (or  $[\overline{201}]$ ) and  $120^{\circ}$  (or  $[0\overline{11}]$ ) orientations showed similar occurrences (53 and 56 counts, respectively), while the 90° orientation exhibited a count of 65 molecules, which is 16%/23% higher than the ones for the other two directions. Assuming the absence of any preferred orientation for CoPc molecules on the Ag(111) surface, the probability of such a scenario occurring for a sampling size of 174 is approximately 15%. This uneven distribution can therefore be a result of random chance; nonetheless, it is more likely that the higher probability of the 90° orientation is not random but rather due to the influence of the standing surface charge waves. We have seen earlier that the peaks of the charge waves, which represent areas of highest surface charge, tend to align parallel to step edges. In the surface area investigated on our sample, the crystal's miscut causes these step edges to roughly follow the 90° direction (cf. Figure 1). This correlation therefore opens the possibility that rather than the overcount at 90° being a random occurrence, it could indicate that molecules near step edges exhibit a tendency to align one of their diagonals parallel to these standing waves. A larger sample size would be needed to clarify this conclusively.

It is worth noting that while our findings regarding the CoPcs aligning strictly with the Ag(111) close-packed directions agree with some previous studies of metal phthalocyanine (MPc) molecules on the same substrate, 50,54 they appear to deviate from others. 55–58 Among these, the experimental studies featuring other orientations may be influenced by the fact that in these, molecules were often located very close to each other forming clusters, which enables neighboring molecules to influence each other's orientations. 66,59 This is not the case in our study, where all molecules included in the count were isolated from each other (Figure 2a). For the theoretical studies using density functional theory (DFT), in particular an orientation that is about 15° off atomic directions has been

identified as favorable, <sup>54,57,58,60</sup> but these calculations suffer from the fact that long-range van der Waals forces are difficult to consider correctly but may influence the equilibrium configurations significantly. <sup>57,61–63</sup> Therefore, to summarize this section, comparing our results with previous findings indicates that since all molecules are oriented equivalently with respect to the geometry of the underlying lattice of the Ag(111), analysis of one molecule will pertain to all with the constraint that details of the analysis may be sensitive to factors related to charge density modulations in the substrate caused by, e.g., intermolecular interactions and proximity to surface defects and impurities.

High-Resolution Single CoPc Molecule 3D-AFM. With the overall adsorption behavior clarified, we moved on to characterizing single molecules using 3D-AFM with a CO molecule at the tip apex.<sup>2,64,65</sup> Figure 3 gives a step-by-step illustration of the procedure that was applied to obtain dense 3D arrays of data points for tip-sample interaction forces and energies in all three dimensions, which included the implementation of a layer-by-layer scanning technique for data acquisition that has been described and analyzed earlier. 4,14,16,66,67 Since recording an individual layer, i.e., an xy map of the frequency shift  $\Delta f$  at a constant height z (cf. the Methods section), takes approximately 30 min, the first decisions an operator has to make are how many layers to include into a data set and at which distances these numbers of layers ought to be collected so that a dense 3D array accurately representing the tip-sample interaction energies and forces can be reconstructed while at the same time data acquisition times are kept as short as possible. While up to 140 equidistant layers acquired over 40 h were used in our initial 3D-AFM studies,<sup>4</sup> we have since found that a much smaller number of low-noise NC-AFM images can suffice if the distance between individual layers is iteratively increased at larger tip-sample distances; as a rule of thumb, the smaller the changes within an AFM image and from one layer to the next, the larger the interlayer distance can be without missing important information. In our present case, we used a 14-layer approach (cf. Figure S1), but we should note that the lowest number of layers that lead to satisfactorily accurate force field reconstruction may be higher for systems that feature more complex force fields.

Even though we used ten times fewer layers than in our initial work, it still took 8 h to complete the data set presented here. While the drift in z direction was found to be negligible within this time frame (see the Accuracy Check section below for details), a certain amount of lateral thermal drift (determined to be ≈30 pm/hour) was unavoidable between layers. To compensate for this drift, we applied the "shift-and-crop" technique introduced earlier<sup>4,66</sup> using the center of the molecule as the reference point. In addition, a  $5 \times 5$  averaging kernel filter was employed to smooth each of the images and to reduce noise before curve fitting was carried out; both steps are illustrated in Figure S2. Combining the filtered, then shifted, and then cropped images into one data set then leads to the creation of the  $\Delta f(x, y, z)$  data array sketched in step 1 of Figure 3. Also note that the combination of the layer-by-layer scanning approach with the postacquisition "shift-and-crop" technique makes it easier to compensate for lateral drift compared to a scheme where individual  $\Delta f(z)$  curves were to be recorded in an (x,y)grid. In that case, drift compensation would need to happen during data recoding by, e.g., atom tracking, 68 which would interrupt the measurement.<sup>67</sup> Another advantage is that the layer-by-layer technique is more efficient in its ability to detect and ultimately avoid tip changes.

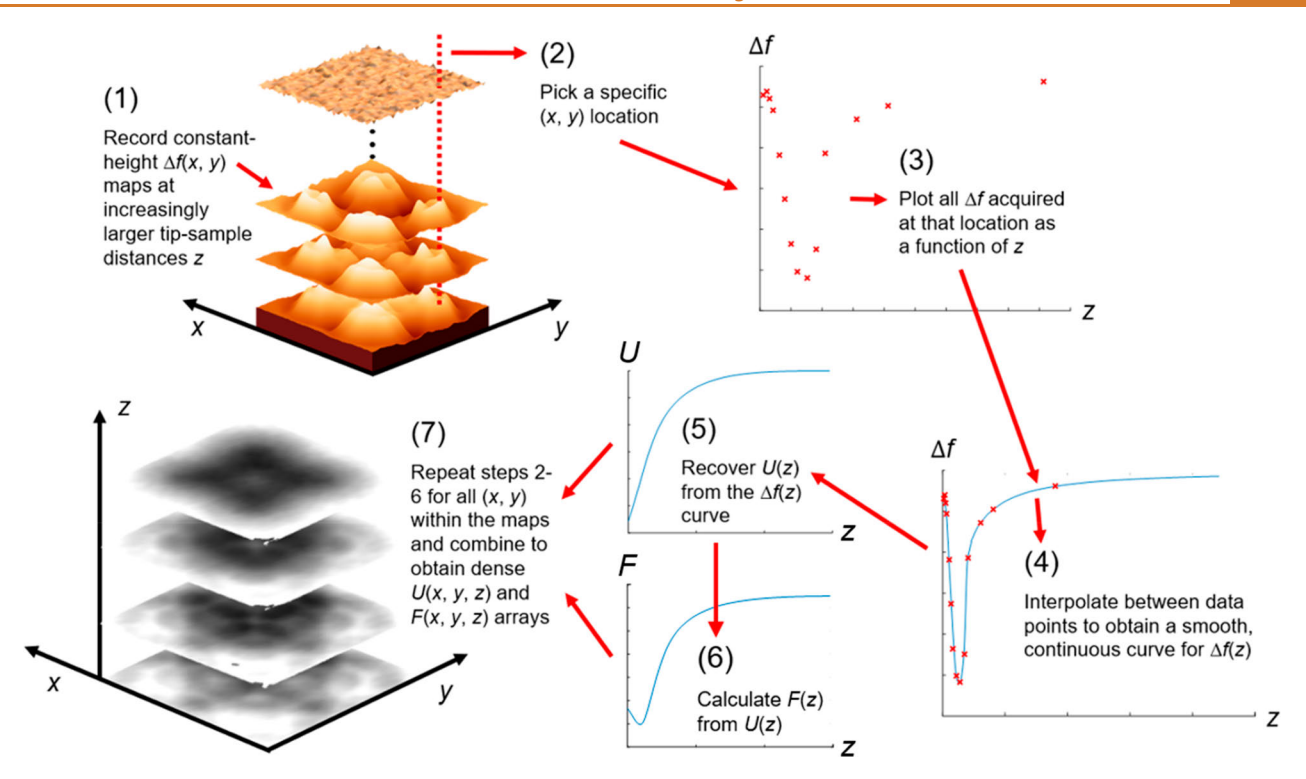


Figure 3. Step-by-step illustration of the procedure applied to obtain dense arrays of data points for tip-sample interaction forces and energies in all three dimensions. For more details, see text.

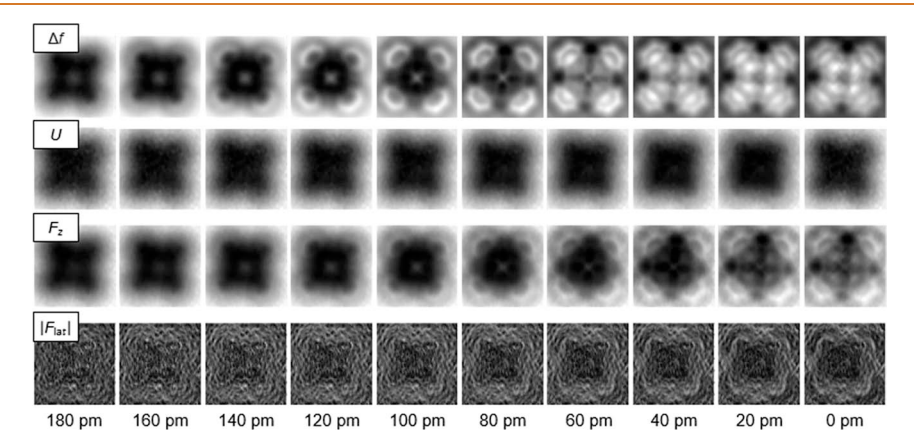


Figure 4. Maps of the frequency shift  $\Delta f$ , potential energy U, vertical force  $F_z$ , and absolute value of the lateral force  $|F_{\rm lat}|$  at different distances z above the CuPc molecule, with z=0 pm indicating the closest distance between tip and sample that is included in the data set. Color scales were adapted in each image based on its maximum and minimum values to optimize the contrast.

While this  $\Delta f(x, y, z)$  data array is sufficiently dense in the x and y directions (145  $\times$  145 pixels over the a total xy image size of  $1.7 \times 1.7$  nm or  $\sim 25$  pixels/Ag lattice constant, which is easily sufficient to reflect the surface corrugation), it only contains  $\Delta f$ values for 14 specific tip-sample distances z (steps 2 and 3 in Figure 3). To create a dense array in z as well, we interpolate the  $\Delta f(z)$  curves between these 14 data points. The interpolation procedure that results in the best match may depend on the nature of the surface force fields investigated, but for the present case, we found that a special type of spline interpolation ("modified Akima interpolation" 69,70) reproduced the shortrange part well while for the long-range part, a simple power curve  $\Delta f = az^b$  delivered good agreement with a and b fit constants. Figure S3 explains how these two parts are merged through the introduction of an intermediate section that is smoothed by a weighted average, which is determined by a data

point's distance to both the short-range and long-range parts. As a result, we obtain for each (x, y) pixel that is part of the 4D data set  $\Delta f$  values in picometer increments in z, with z running from 0 to 20 Å (i.e., 2000 data points in total; see step 4).

Once dense  $\Delta f(z)$  curves were available, they were converted to potential energy U vs z curves (cf. step 5) via the following equation:  $^{71-73}$ 

$$U(z) = \frac{2k}{f_0} \int_z^\infty \Delta f \left[ (t - z) + \sqrt{\frac{A(t - z)}{16\pi}} + \frac{A^{3/2}}{\sqrt{2(t - z)}} \right] dt$$

$$(1)$$

where k is the spring constant of the force sensor (in our case a quartz tuning fork in the qPlus configuration<sup>6,74,75</sup>),  $f_0$  is the

resonance frequency of the tuning fork when the tip is far from the surface, A is the oscillation amplitude of the tip, z is the specified distance of interest, and t is the integration variable (distance). Normal (i.e., vertical) forces  $F_z$  and lateral forces  $F_{lat}$ (i.e., the magnitude of the forces acting within the xy plane) were then recovered in step 6 of Figure 3 by

$$F_z = -\frac{\partial U}{\partial z} \tag{2}$$

and

$$F_{\text{lat}} = \sqrt{\left(\frac{\partial U}{\partial x}\right)^2 + \left(\frac{\partial U}{\partial y}\right)^2} \tag{3}$$

This ultimately leads to the availability of dense fourdimensional data sets for  $\Delta f(x, y, z)$ , U(x, y, z),  $F_z(x, y, z)$ , and  $F_{lat}(x, y, z)$ , with Figure 4 showing constant-height maps of all four of these quantities at the tip-sample distances given at the bottom of the figure; note that z is calibrated to zero at the closest tip-sample distance included in the data set and therefore does not represent an absolute value for the tipsample distance. While the frequency shift and normal force images demonstrate a conspicuous alteration of contrast with changes in height, the potential and lateral force images do not exhibit prominent changes. It might also be noteworthy that the lateral force maps exhibit a squared contour for the molecule despite its cross-shaped molecular structure. For better visibility, we have produced vector-based maps of the lateral forces; two examples at tip-sample distances of 0 and 80 pm are displayed in Figure S4. In addition, two videos produced from the 4D data sets are included, with one showing the frequency shift as a function of the tip—sample distance z and the other one showing the normal force (Video 1 and Video 2), both of which provide detailed insight into how the tip-sample interaction changes with increasing tip—sample distance.

Accuracy Check and Removal of Substrate Influence. Since we are using an interpolation process to increase the number of data points for  $\Delta f$  in the z direction from an initial 14 to 2000, one could be concerned about how precise this interpolation matches the distant-dependent behavior of the actual frequency shift data. To ensure the accuracy of our interpolated images, we have performed control experiments by collecting densely spaced (in z) frequency shift vs distance curves at various symmetry locations on the molecule as well as on the bare substrate. These curves, which contained 2500 data points each over their 20 Å range, were then compared with our interpolated frequency shift data; three examples of such curves are provided in Figure 5. We find that even though the fit has been reconstructed from only 14 data points with the one most distant from the surface at z = 9 Å, the fit reproduces the measured  $\Delta f(z)$  curves at all three locations with excellent precision up to 20 Å, which was the furthest distance we included in the data set. This exceptional match between interpolated curves and experimentally measured  $\Delta f(z)$  at the same locations leads us to conclude that the postinterpolation data set for  $\Delta f(x, y, z)$  exhibits a high level of accuracy; as a consequence, we expect the same to apply for the U(x, y, z),  $F_z(x, y, z)$ , and  $F_{lat}(x, y, z)$  data sets as well. In addition, it also implies that drift in the z direction was negligible within the 8 h of measuring time. To achieve such a low drift, the system was allowed to stabilize at 5 K for 2+ days prior to the measurements with the windows of the thermal shields closed while the *x*, *y*, and

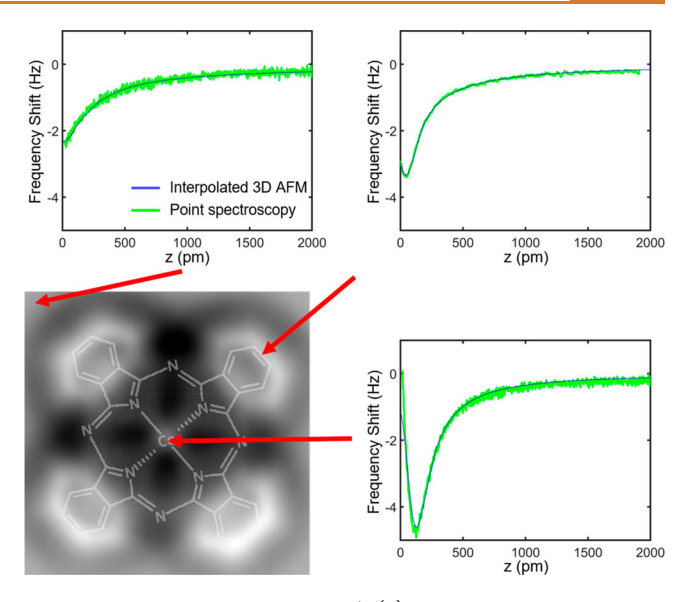


Figure 5. Comparison between  $\Delta f(z)$  curves obtained through interpolation from the layer-by-layer imaging scheme described in the previous section (blue) and dense unfiltered experimental  $\Delta f(z)$ data (green) recorded at two different symmetry locations on the molecule (on a lobe, upper-right curve, and on the center Co atom, lower-right curve) and on the substrate (upper-left curve) that are indicated in the  $\Delta f(x, y)$  constant-height map displayed in the lower left of the figure. A structural model of a CoPc has been overlaid with the data; to guide the eye, it has been scaled to fit the molecule's apparent size. 42,76

z voltages on the scan piezo were kept between -10 and 0 V to eliminate piezo creep.

While for any measurements using scanning probe microscopy, molecules have to be supported by a substrate, it is in many cases the force exerted by the molecule alone (i.e., without the substrate contribution) that is of interest for chemical insight. To account for such circumstances, we generated a modified data array  $F_z^{\text{tip-CoPc}}(x, y, z)$  representing the tip-molecule contribtions to the total force only, which was obtained by subtracting the force attributed to the tip-substrate interaction  $F_z^{\mathrm{tip-Ag}}(z)$  from the total tip—sample forces  $F_z$  measured across the molecule (i.e.,  $F_z^{\mathrm{tip-Co^pc}}(x,y,z) = F_z(x,y,z) - F_z^{\mathrm{tip-Ag}}(z)$ ). Assuming additivity of forces (cf. ref 77), this is straightforward to implement. To obtain an accurate "generic" tip-substrate force  $F_z^{\text{tip-Ag}}(z)$  suitable for subtraction at each (x, y) coordinate, 25 substrate force curves acquired away from the molecule at each corner of the (x, y) field of view were selected and averaged. The effect of this manipulation is presented in Figure 6 with the example of five  $F_z^{\text{tip-CoPc}}(z)$  curves that have been obtained on characteristic symmetry locations of CoPc (plotted in blue); each of the curves is contrasted to the original  $F_z(z)$  curve at the same location (green). Most notably, we find that upon subtracting the average substrate forces from the force curves obtained over the CoPc molecule, distinct minima emerge in the curves that represent the tip-molecule force only. This observation suggests that the repulsive forces between the probe and the molecule begin to dominate over the attractive forces exerted by the molecule at distances larger than what might have been inferred from the analysis of the raw  $F_z(z)$ curves. Differently stated, attractive forces from the substrate may overshadow repulsive tip-molecule forces, making them less apparent in the original force curves as they are masked by elastic deformation in both the CoPc and tip (such as through

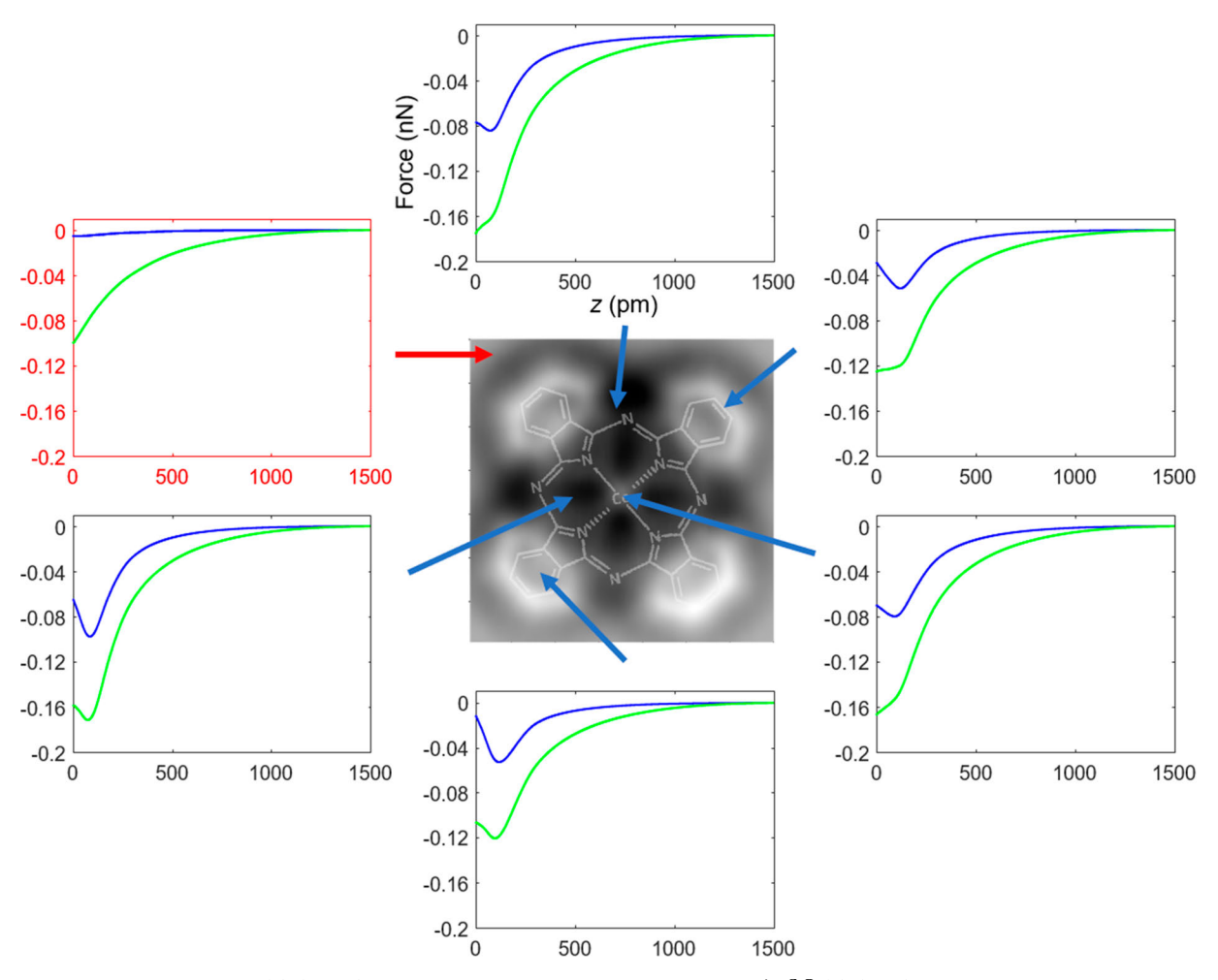


Figure 6. Original force curves  $F_z(z)$  (green) and background-subtracted force curves  $F_z^{\text{tip-CoPc}}(z)$  (blue) obtained at different locations on the CoPc molecule; the locations where each curve was recorded are indicated in the center  $\Delta f(x,y)$  constant-height map (structural model overlaid and scaled as in Figure 5). The curve in the upper left (red frame), which is positioned away from the substrate, is included for control purposes: when subtracting the averaged background tip—substrate force  $F_z^{\text{tip-Ag}}(z)$  from the  $F_z(z)$  curve that was acquired at this exact pixel (green), the resulting blue curve is almost identical to zero at all distances, showing that the quality of the generic tip—substrate force curve is indeed sufficient to assemble a highly accurate  $F_z^{\text{tip-CoPc}}(x,y,z)$  data array.

tilting of the terminating CO molecule). A video of the subtracted force maps  $F_z^{\text{tip-CoPc}}(x, y)$  changing with z has been provided (Video 3).

Equilibrium Potential Determination. At this point, we have recovered highly accurate, dense  $F_z(x, y, z)$ ,  $F_{lat}(x, y, z)$ , and  $F_z^{\text{tip-CoPc}}(x, y, z)$  data arrays. However, it is the potential at the equilibrium bonding distance that provides the most insight into the energetics of surface chemical reactions. For the present case study, the parameter of greatest interest to retrieve with respect to the CO<sub>2</sub>-to-methanol conversion reaction catalyzed by the CoPcs is the equilibrium potential energy of an adsorbed CO molecule that forms as an intermediary product. In a first step toward that goal, we note that the  $F_z^{\text{tip-CoPc}}(x, y, z)$  data set allows for determination of the minimum attractive force  $F_z^{\text{tip-CoPc, min}}$ at each (x, y) pixel and to subsequently plot this value in a minimum force map (Figure 7a). Since the tip is terminated by a CO molecule during data acquisition and tip-molecule interactions decay quickly with distance, we can regard this  $F_{x}^{\text{tip-CoPc, min}}(x,y)$  force map as a rough first-order approximation of the forces felt by a CO molecule approaching CoPc, i.e.,  $F_z^{\text{tip-CoPc, min}}(x, y) \approx F_z^{\text{CO(ad)-CoPc}}(x, y)$ . Another issue that contributes to making this equivalence rough is that the CO molecule terminating the tip is "flipped" compared to a CO that

would be adsorbed to the molecule; i.e., the tip-attached CO has its oxygen pointing toward the CoPc while a reactive CO during conversion would attach to the center cobalt atom with its carbon-terminated end. Even though these two simplifications will cause the numerical values specified in the  $F_z^{\text{tip-CoPc}}$ ,  $\min(x, y)$  force map to deviate from what a "free" CO will encounter when adsorbing on the CoPc, we still expect the  $F_z^{\text{tip-CoPc}}$ ,  $\min(x, y)$  map to provide useful insight into both the degree of force fluctuations occurring with changes in the (x, y) position and the general overall strength of the local CoPc—CO interaction.

The objective of this section is, however, to estimate the equilibrium potential of an adsorbed CO molecule, which occurs at the distance where  $F_c^{\rm CO(ad)-CoPc}$  is zero. Unfortunately, recovery of the related  $U_c^{\rm CO(ad)-CoPc,min}(x,y)$  map is challenging because at the tip—sample distance at which  $U_c^{\rm tip-CoPc}$  is at its minimum, substantial repulsive forces act that deform both the tip and the molecule. Thereby, deformations in the tip may primarily manifest as a tilting of the CO that is attached to the tip's apex 42,76,78,79 while in the sample, we can expect that the locally repulsive forces exerted by the tip push the CoPc closer toward the substrate, which locally reduces the CoPc—Ag distance and causes the molecule to bend or tilt. Either way, such deformations will alter the measured tip—CoPc interaction from

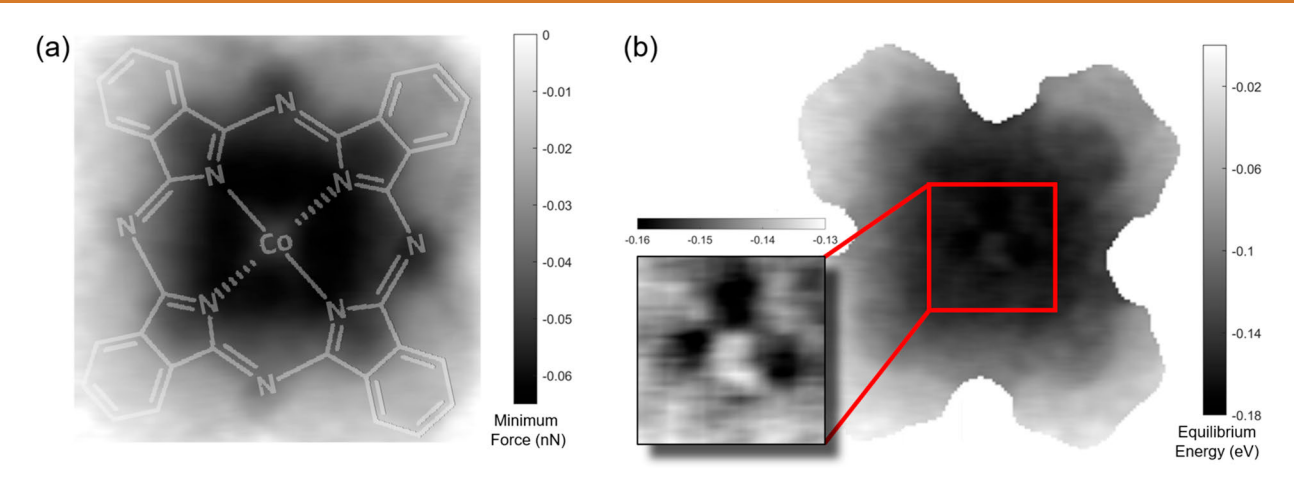


Figure 7. (a) Minimum force map  $F_z^{\rm tip-CoPc,min}(x,y)$  obtained from the full  $F_z(x,y,z)$  data array after (i) subtracting the generic tip—substrate force  $F_z^{\rm tip-Ag}(z)$  generated by averaging tip—substrate curves recorded at various locations away from the molecule and then (ii) plotting the value of the most attractive force value at each (x,y) pixel. (b) Map of the equilibrium energy  $\varepsilon$  recovered using the fit procedure explained in the main text with d=3.2 Å. For better visibility of the potential landscape around the center cobalt atom, which is the decisive factor for  ${\rm CO}_2$  to methanol conversion, a zoomed-in inset was added where the color scale covers a reduced energy range from -0.16 eV (darker colors) to -0.13 eV (brighter colors). Note that the potential minimum is not right on top of the cobalt but to its side. From the inset, which has been added for better visibility, we can see that only three of the four sites where one would expect the potential minimum based on symmetry considerations show a well-developed minimum. Possible reasons for this finding can be either a slightly asymmetric placement of the molecule on the substrate or a tip asymmetry.

the value a CO molecule adsorbing on the CoPc would experience, i.e.,  $U^{\rm tip-CoPc,min} \neq U^{\rm CO(ad)-CoPc,min}$ , even if we ignore the issue with the CO being "flipped". To make things worse,  $U^{\rm tip-CoPc,min}$  is difficult to measure, as the repulsive forces acting at that distance may cause the tip to permanently change, typically losing its terminating CO molecule in the process. As a result, the force—distance curves composing the experimental  $F_z^{\rm tip-CoPc}(x,y,z)$  data array do not extend all the way to the distance where  $F_z^{\rm tip-CoPc}$  is zero; to protect the tip, the distance of closest approach included in the data array, which we have defined as z=0 for convenience (cf. Figure S1), is set before such value is reached.

To overcome these obstacles, we implemented another fitting procedure that *estimates* the  $U^{\rm CO(ad)-CoPc,min}(x,\ y)$  potential landscape that an adsorbing CO molecule encounters. The procedure relies on two assumptions:

1. First, we assumed that the tip—CoPc interaction potential follows a modified Lennard-Jones-type behavior where the repulsive part scales with the power of 12 while the attractive part is allowed to scale with a power law that deviates from the factor of 6 commonly used in Lennard-Jones-type potentials. 80,81 This assumption is motivated by the fact that the CO molecule terminating the probe tip is "sticking out" from the otherwise metallic tip, which causes the repulsive forces felt first to be almost exclusively caused by the interaction of the foremost tip atom (oxygen in this case) with the CoPc. The metal atoms "further back" in the tip (i.e., behind the CO) will, however, contribute to some degree to the more longer-range attractive forces, 82 which can be considered in a model interaction by reducing the related exponent to values lower than 6.83 This approach also follows prior work that showed that density functional theory calculations of the interactions between CO-terminated tips and surfaces could be modeled through additive pairwise interactions<sup>84</sup> and that frequency shift vs distance data for such tips could also be fit to Lennard-Jones-type

potentials. <sup>85</sup> Referring to this factor as *g*, we can write for the resulting modified Lennard–Jones potential

$$U^{\text{LJ,mod}}(z) = \varepsilon \left[ \left( \frac{g}{12} \right)^{g/(12-g)} - \left( \frac{g}{12} \right)^{12/(12-g)} \right]^{-1}$$
$$\left[ \left( \frac{\sigma}{z+d} \right)^{12} - \left( \frac{\sigma}{z+d} \right)^{g} \right] \tag{4}$$

To conform with common practice,  $-\varepsilon$  represents the minimum energy and  $\sigma$  the distance (z+d) where the energy is zero; note that for the latter, the distance scale is defined by the LJ potential. Since z remains calibrated to the smallest tip—CoPc distance in the data set, we have to introduce the parameter d, which adjusts the denominator so that  $U^{\mathrm{LJ,mod}}(-d) \to \infty$ . From eq 4, we then obtain by derivation the corresponding force law

$$F_z^{\text{LJ,mod}}(z) = \frac{\varepsilon}{\sigma} \left[ \left( \frac{g}{12} \right)^{g/(12-g)} - \left( \frac{g}{12} \right)^{12/(12-g)} \right]^{-1}$$
$$\left[ 12 \left( \frac{\sigma}{z+d} \right)^{13} - g \left( \frac{\sigma}{z+d} \right)^{g+1} \right] \tag{S}$$

2. For the fit, we then assumed that the experimental data is only reliable up to the point where  $F_z^{\rm tip-CoPc}(z)$  is at its minimum, as past this point, the emergence of repulsive forces causes the tip and the sample to deform, causing the measured curve to deviate from what an individual CO molecule would experience if exposed to the CoPc's surface potential.

The fitting procedure is illustrated in Figure S5; essentially, we fit eq 5 to the experimental data  $F_z^{\text{tip-CoPc}}(z)$  down to the minimum and then use the set of fit parameters recovered (i.e., d, g,  $\sigma$ , and  $\varepsilon$ ) to extrapolate the curve to where  $F_z^{\text{LJ,mod}}(z)$  becomes zero, which is at

$$r_{\rm eq} = (z + d)_{U=U_{\rm min}} = \left(\frac{12}{g}\right)^{1/(12-g)} \sigma$$
 (6)

where  $r_{\rm eq}$  then represents a "best estimate" for the CO–CoPc equilibrium distance on the distance scale defined by the LJ potential. In this context, four observations are noteworthy:

- 1. During the fitting process, it was observed that several distinct sets of d, g, and  $\sigma$  accurately represented the experimental  $F_z^{\rm tip-CoPc}(z)$  curve down to its minimum. To address this, we started by assigning a reasonable but fixed value to d and then fit the remaining three parameters; values between d = 3.2 and 3.65 Å were chosen to reproduce the expected van der Waals (vdW) diameters  $\sigma$ . The tabulated values for  $\sigma$  for each element vary depending on the exact environment, with typical values for C, N, and Co centered around 3.9, 3.6, and 4.0 Å, respectively.<sup>86</sup> Meanwhile, a value of 3.02 Å has been determined for O in CO.87 We found that regardless of the value set for d, the fitting process consistently converged to nearly identical equilibrium energies  $\varepsilon$  at each point, which could be plotted in an equilibrium energy map  $U^{CO(ad)-CoPc,min}(x, y)$  (Figure 7b and middle column of Figure S6). Interestingly, the adsorption strength adjacent to the cobalt appears to be somewhat stronger than directly above the Co, exhibiting a three-pointed structure (see inset in Figure 7b).
- 2. Maps of the equilibrium distance  $r_{\rm eq}$  calculated from eq 6 also remained virtually unaffected if taken relative to the lowest level or approach included in the data set, i.e., variations in the  $r_{\rm eq}$  map are invariant with respect to d and thus accurately measured even though the absolute distance d is uncertain (cf. Figure S6, left column).
- 3. The choice of *d* does, however, affect the value of *g*, with lower values of *d* leading to lower *g* (see caption of Figure S6 for a quantitative assessment of this effect).
- 4. Equilibrium distances recovered from this fitting procedure are, as reported in Figure S6, all within the first one angstrom of the z range covered by the data set even though the experimentally obtained data does not reach the  $F_z^{\text{tip-CoPc}}(z) = 0$  point. This is due to the substantial deformation that both tip and sample undergo (see Figure S5), which is the underlying reason why this fitting procedure is necessary.

Several important insights emerge from the data that can be extracted, in particular, with respect to the nature of the interactions of carbon monoxide with immobilized CoPc. First, the lack of knowledge of the absolute tip—sample distance constrains what can be *a priori* quantitatively gleaned from the data. For example, the effective atomic diameters and decay exponent of the attractive interaction are not accessible without prior estimates of the atomic diameters. Meanwhile, variations in the equilibrium bonding distances can still be quantitatively obtained, but the absolute scale also depends on estimates of the atomic diameters. On the other hand, the most important parameter, the equilibrium bonding energy, is insensitive to the calibration of the tip—sample distance and can be quantitatively determined without prior knowledge of the atomic diameters.

Regarding the CoPc–CO interaction, the interaction with the CO oxygen atom falls within the nonbonding physisorption range and maximizes at less than 160 meV, even though a stronger interaction is anticipated when the Co center is reduced, as is the case during electrochemical  $CO_2$  reduction.<sup>37</sup>

As would be expected, the interaction is weakest at the aromatic hydrogens. Surprisingly, the strongest interaction is not directly over the Co atom but rather in pockets surrounding it. A consensus has emerged that the highest occupied molecular orbital for isolated CoPc is an A<sub>1g</sub> orbital concentrated above the Co atom; 88,89 indications are that this does not change drastically when adsorbed on a Au(111) surface. On the other hand, the lowest unoccupied orbitals are concentrated adjacent to the Co atom in two degenerate  $e_{\mbox{\tiny g}}$  orbitals. <sup>88,89</sup> The implication from the data is then that the CO oxygen atom exhibits greater attraction to the LUMO. 88 Alternatively, Ellner et al.<sup>84</sup> previously found that the CO-metal tip system can be described as a negative point charge surrounded by a diffuse positive charge. This finding could potentially explain the observation that the interaction strength does not peak above the Co atom as well, even though we also need to consider that at the distances where the attractive interaction energy is greatest, Pauli repulsion governs the interaction. Further, an electrostatic argument would suggest a central depression at the Co atom surrounded by a ring, which was, however, not observed.

Over the past decade or so, CO has emerged as the *go-to* molecule for tip functionalization for high-resolution SPM imaging of molecular structures. <sup>2,5,39–42</sup> We have shown here that this approach can yield quantitative atom-resolved data on the strength of intermolecular interactions. A limitation is that the CO is inverted compared with its preferred orientation for adsorption on most surfaces and molecular catalysts. Carbon monoxide, however, is not the only possible tip termination that can provide high-resolution images. <sup>91</sup> Thus, looking forward, we call on researchers to design tips to specifically probe the specific chemical interactions that are important to the processes of interest.

## **CONCLUSIONS**

Locally characterizing parameters such as the interaction force and energies an individual supported catalytic molecule may exhibit toward an incoming reactant bears great potential to spur targeted progress in catalysis research. For this specific case study, CoPc molecules adsorbed on Ag(111) were chosen as they have recently been shown to represent a promising class of hybrid catalysts that promote the production of methanol from CO<sub>2</sub>, with scientific interest focused on a detailed understanding of how the adsorption strength of the central cobalt atom toward intermediate carbon monoxide molecules can be fine-tuned to promote the most efficient reaction. This paper has demonstrated the capabilities of scanning probe microscopy methodology in recovering tip-sample interactions with picometer accuracy in all three spatial dimensions. By employing a lowtemperature, ultrahigh vacuum scanning probe microscope in combination with postacquisition data analysis procedures, we have successfully generated detailed three-dimensional maps of the interaction between cobalt phthalocyanine (CoPc) molecules deposited on an Ag(111) surface and a probe microscopy tip terminated by a single carbon monoxide molecule. Lack of knowledge of the absolute tip—sample distance makes it difficult to recover all of the parameters of the local interaction potentials, but nonetheless, variations in the equilibrium bond length between the tethered CO and CoPc could still be determined with high accuracy. The uncertainty in the absolute tip-sample distance, however, did not impact the ability to consistently recover the equilibrium bonding strength  $\varepsilon$  between the CO-terminated tip and the CoPc molecule at every point; on average,  $\varepsilon$  varied by only about 0.1% for most points within the

range of values considered for *d*. The CO molecule attached to the tip is inverted compared to its preferred adsorption geometry on CoPc with the C atom closest to the cobalt atom. In this configuration, CO—CoPc interactions fall in the physisorption regime with a peak attractive energy of less than 160 meV. This peak does not occur directly over the Co atom but rather in pockets surrounding it, suggesting that the CO oxygen most strongly interacts with the unoccupied electronic states concentrated adjacent to the Co atom.

#### **METHODS**

**Experimental Apparatus.** Measurements were performed with a CreaTec-based low-temperature scanning tunneling microscope system (CreaTec Fischer & Co. GmbH, Berlin, Germany) custom upgraded with high-resolution atomic force microscopy (HR-AFM) capability and operated using the open-source GXSM control software. Page The ultrahigh vacuum (UHV) system had a base pressure of  $7 \times 10^{-11}$  Torr. The qPlus sensor used for this work featured a resonance frequency  $f_0$  of 30,210 Hz, a spring constant k of  $\sim 1800$  N/m, and a quality factor of  $\sim 10,000$  when being far away from the surface. A 25  $\mu$ m diameter platinum—iridium wire, cut and sharpened by focused ion beam milling, was attached to the qPlus sensor as the tip. Sefore being mounted on the SPM scanner, the tip was cleaned by Ar+ sputtering from three directions in UHV. The final metal tip apex shaping was then performed *in situ* via controlled nanoindentations into the silver crystal substrate accompanied by bias pulsing.

Sample Preparation. The Ag(111) single crystal substrate was prepared by four cycles of Ar<sup>+</sup> sputtering followed by annealing; in each cycle, sputtering was carried out for 15 min with a sputtering current of  $5 \,\mu\text{A}$  at a voltage of 1 kV followed by annealing up to 550 °C for another 15 min. The substrate was then inserted into the microscope and cooled down to 5 K. CoPc powder purchased from Sigma-Aldrich (Sigma-Aldrich, MO, USA) was placed in an evaporator that consisted out of a silicon carrier substrate heated by direct current. Once the loaded evaporator was mounted to the vacuum chamber, the CoPc source material was purified by a brief predeposition sublimation with the doors of the cryostat's thermal shield closed, which causes volatile impurities to leave the powder without being able to hit the sample. This was followed by the actual deposition process, during which the shield's door was opened for about 10 s so that CoPc molecules could reach the cold surface of the silver crystal; in this context, please note that the radiation exposure associated with the open doors caused the silver substrate's temperature to rise to about 10  $\bar{\text{K}}$ . The resulting CoPc coverage was approximately 1 molecule/75 nm<sup>2</sup>, which was suitable for our experimental purposes.

**Tip Functionalization.** The CO molecules used to functionalize the tip apex were dosed onto the surface with the sample at 5 K. Thereby, CO exposure was achieved by opening the cryostat door for 10 s with a CO pressure of  $2\times 10^{-8}$  Torr in the main chamber. For the tip to pick up a CO molecule from the Ag(111) surface, consecutive scans in STM mode with a bias of a few mV and various currents up to 50 pA were carried out over a CO molecule. This caused the tip to be in very close proximity to the CO and eventually resulted in the transfer of the CO molecule to the very end of the tip apex, as determined by the disappearance of a CO molecule in the STM images and a change in STM contrast. As detailed in the experimental apparatus section, the tip is prepared by controlled nanoindentation resulting in Ag at the tip apex; thus, CO is considered to be bound to Ag on the tip. The CO–Ag interaction is a weak physisorption interaction.

Three-Dimensional High-Resolution Atomic Force Microscopy. All raw data used to create the three-dimensional force and energy data sets were recorded in constant-height mode, while a bias voltage of 20 mV was applied between tip and sample, which allowed simultaneous collection of a tunneling current. Tip oscillation amplitudes were ~60 pm, and a custom high-speed GXSM Red-Pitaya—PAC-PLL controller was used to detect the frequency of the tip oscillation. Once molecules of interest were found, a layer-by-layer imaging strategy was utilized as originally outlined in ref 4.

Measurements always started with the closest distance to the molecule and then increasingly larger distances in subsequent runs, with the point of closest approach for the data set determined by the distance at which the tunneling current saturated. During data acquisition, the frequency shift  $\Delta f = f - f_0$  (where  $f_0$  is the qPlus sensor's resonance frequency when the tip is far away from the surface and f its resonance frequency at the spatial location (x, y, z) probed), the tunneling current I, the oscillation amplitude of the tip A, and the phase difference  $\phi$  between the signal driving the qPlus sensor and its actual oscillation were tracked simultaneously. After a complete layer at a constant height z had been recorded for the xy field of view chosen, the tip was moved away from the molecule by a certain distance, and the same procedure was repeated. For the closest tip-sample distances, the move-away distance between layers was set to 10 pm but was increased to larger values as the tip moved away from the molecule (Figure S3). A typical scan time for one image with a  $512 \times 512$  pixels resolution was 30 min.

#### ASSOCIATED CONTENT

# Supporting Information

The Supporting Information is available free of charge at https://pubs.acs.org/doi/10.1021/acsnano.3c11219.

Figures showing (1) constant-height frequency shift maps acquired at different heights; (2) the data interpolation procedures used and associated results; and (3) lateral force maps acquired at two different tip—sample distances (PDF)

# **Web-Enhanced Features**

Videos 1, 2, and 3 showing the frequency shift as a function of the tip—sample distance z, the normal force, and the subtracted force maps  $F_z^{\text{tip}-\text{CoPc}}(x, y)$  changing with z, respectively.

# **AUTHOR INFORMATION**

# **Corresponding Author**

Udo D. Schwarz — Department of Mechanical Engineering and Materials Science and Department of Chemical and Environmental Engineering, Yale University, New Haven, Connecticut 06511, United States; ◎ orcid.org/0000-0002-5361-0342; Email: udo.schwarz@yale.edu

#### Authors

Xinzhe Wang — Department of Mechanical Engineering and Materials Science, Yale University, New Haven, Connecticut 06511, United States

Percy Zahl — Center for Functional Nanomaterials, Brookhaven National Lab, Upton, New York 11973, United States; orcid.org/0000-0002-6629-7500

Hailiang Wang — Department of Chemistry, Yale University, New Haven, Connecticut 06511, United States; orcid.org/ 0000-0003-4409-2034

Eric I. Altman — Department of Chemical and Environmental Engineering, Yale University, New Haven, Connecticut 06511, United States; orcid.org/0000-0003-4032-271X

Complete contact information is available at: https://pubs.acs.org/10.1021/acsnano.3c11219

## Notes

The authors declare no competing financial interest.

## **ACKNOWLEDGMENTS**

This work has been supported by the National Science Foundation through Grant CHE-2203589. Any opinions, findings, and conclusions or recommendations expressed in this material are those of the author(s) and do not necessarily

reflect the views of the National Science Foundation. Initial results were made possible by a seed grant provided by the Yale Planetary Solutions Project. This research used the LT-STM/NC-AFM facility of the Center for Functional Nanomaterials (CFN), which is a U.S. Department of Energy Office of Science User Facility, at Brookhaven National Laboratory under Contract DE-SC0012704.

## **REFERENCES**

- (1) Gross, L.; Moll, N.; Mohn, F.; Curioni, A.; Meyer, G.; Hanke, F.; Persson, M. High-Resolution Molecular Orbital Imaging Using a p-Wave STM Tip. *Phys. Rev. Lett.* **2011**, *107* (8), 086101.
- (2) Gross, L.; Mohn, F.; Moll, N.; Liljeroth, P.; Meyer, G. The Chemical Structure of a Molecule Resolved by Atomic Force Microscopy. *Science* **2009**, 325 (5944), 1110–1114.
- (3) Chiang, C. L.; Xu, C.; Han, Z.; Ho, W. Real-space imaging of molecular structure and chemical bonding by single-molecule inelastic tunneling probe. *Science* **2014**, *344* (6186), 885–888.
- (4) Albers, B. J.; Schwendemann, T. C.; Baykara, M. Z.; Pilet, N.; Liebmann, M.; Altman, E. I.; Schwarz, U. D. Three-dimensional imaging of short-range chemical forces with picometre resolution. *Nat. Nanotechnol* **2009**, *4* (5), 307–310.
- (5) Gross, L.; Schuler, B.; Pavlicek, N.; Fatayer, S.; Majzik, Z.; Moll, N.; Pena, D.; Meyer, G. Atomic Force Microscopy for Molecular Structure Elucidation. *Angew. Chem., Int. Ed. Engl.* **2018**, *57* (15), 3888–3908.
- (6) Giessibl, F. J. The qPlus sensor, a powerful core for the atomic force microscope. *Rev. Sci. Instrum.* **2019**, *90* (1), No. 011101.
- (7) Kaiser, U.; Schwarz, A.; Wiesendanger, R. Magnetic exchange force microscopy with atomic resolution. *Nature* **2007**, 446 (7135), 522–525
- (8) Kazakova, O.; Puttock, R.; Barton, C.; Corte-Leon, H.; Jaafar, M.; Neu, V.; Asenjo, A. Frontiers of magnetic force microscopy. *J. Appl. Phys.* **2019**, *125* (6), 060901.
- (9) Soergel, E. Piezoresponse force microscopy (PFM). J. Phys. D Appl. Phys. **2011**, 44 (46), 464003.
- (10) Mascaro, A.; Miyahara, Y.; Enright, T.; Dagdeviren, O. E.; Grutter, P. Review of time-resolved non-contact electrostatic force microscopy techniques with applications to ionic transport measurements. *Beilstein J. Nanotechnol* **2019**, *10*, 617–633.
- (11) Ternes, M.; Lutz, C. P.; Hirjibehedin, C. F.; Giessibl, F. J.; Heinrich, A. J. The force needed to move an atom on a surface. *Science* **2008**, 319 (5866), 1066–1069.
- (12) Ruschmeier, K.; Schirmeisen, A.; Hoffmann, R. Atomic-scale force-vector fields. *Phys. Rev. Lett.* **2008**, *101* (15), No. 156102.
- (13) Such, B.; Glatzel, T.; Kawai, S.; Koch, S.; Meyer, E. Three-dimensional force spectroscopy of KBr(001) by tuning fork-based cryogenic noncontact atomic force microscopy. *J. Vac Sci. Technol. B* **2010**, 28 (3), C4B1.
- (14) Baykara, M. Z.; Schwendemann, T. C.; Altman, E. I.; Schwarz, U. D. Three-dimensional atomic force microscopy taking surface imaging to the next level. *Adv. Mater.* **2010**, 22 (26–27), 2838–2853.
- (15) Fukuma, T.; Ueda, Y.; Yoshioka, S.; Asakawa, H. Atomic-Scale Distribution of Water Molecules at the Mica-Water Interface Visualized by Three-Dimensional Scanning Force Microscopy. *Phys. Rev. Lett.* **2010**, *104* (1), 016101.
- (16) Baykara, M. Z.; Schwendemann, T. C.; Albers, B. J.; Pilet, N.; Monig, H.; Altman, E. I.; Schwarz, U. D. Exploring atomic-scale lateral forces in the attractive regime: a case study on graphite (0001). *Nanotechnology* **2012**, 23 (40), No. 405703.
- (17) Moreno, C.; Stetsovych, O.; Shimizu, T. K.; Custance, O. Imaging three-dimensional surface objects with submolecular resolution by atomic force microscopy. *Nano Lett.* **2015**, *15* (4), 2257–2262.
- (18) Baykara, M. Z.; Monig, H.; Schwendemann, T. C.; Unverdi, O.; Altman, E. I.; Schwarz, U. D. Three-dimensional interaction force and tunneling current spectroscopy of point defects on rutile TiO2(110). *Appl. Phys. Lett.* **2016**, *108* (7), 071601.

- (19) Fukuma, T.; Garcia, R. Atomic- and Molecular-Resolution Mapping of Solid-Liquid Interfaces by 3D Atomic Force Microscopy. *ACS Nano* **2018**, *12* (12), 11785–11797.
- (20) Berwanger, J.; Polesya, S.; Mankovsky, S.; Ebert, H.; Giessibl, F. J. Atomically Resolved Chemical Reactivity of Small Fe Clusters. *Phys. Rev. Lett.* **2020**, *124* (9), No. 096001.
- (21) Langewisch, G.; Falter, J.; Fuchs, H.; Schirmeisen, A. Forces during the controlled displacement of organic molecules. *Phys. Rev. Lett.* **2013**, *110* (3), No. 036101.
- (22) Somorjai, G. A.; Li, Y. Impact of surface chemistry. *Proc. Natl. Acad. Sci. U. S. A.* **2011**, *108* (3), 917–924.
- (23) Jackson, M. N.; Surendranath, Y. Molecular Control of Heterogeneous Electrocatalysis through Graphite Conjugation. *Acc. Chem. Res.* **2019**, 52 (12), 3432–3441.
- (24) Zheng, Y.; Qi, D. C.; Chandrasekhar, N.; Gao, X. Y.; Troadec, C.; Wee, A. T. S. Effect of molecule-substrate interaction on thin-film structures and molecular orientation of pentacene on silver and gold. *Langmuir* **2007**, 23 (16), 8336–8342.
- (25) Yu, C. J.; von Kugelgen, S.; Laorenza, D. W.; Freedman, D. E. A Molecular Approach to Quantum Sensing. *ACS Cent Sci.* **2021**, *7* (5), 712–723.
- (26) Melville, O. A.; Lessard, B. H.; Bender, T. P. Phthalocyanine-Based Organic Thin-Film Transistors: A Review of Recent Advances. *ACS Appl. Mater. Interfaces* **2015**, *7* (24), 13105–13118.
- (27) Verma, C.; Ebenso, E. E.; Quraishi, M. A.; Rhee, K. Y. Phthalocyanine, naphthalocyanine and their derivatives as corrosion inhibitors: A review. *J. Mol. Liq.* **2021**, 334, 116441.
- (28) De Annunzio, S. R.; Costa, N. C. S.; Mezzina, R. D.; Graminha, M. A. S.; Fontana, C. R. Chlorin, Phthalocyanine, and Porphyrin Types Derivatives in Phototreatment of Cutaneous Manifestations: A Review. *Int. J. Mol. Sci.* **2019**, *20* (16), 3861.
- (29) Rezaee, E.; Khan, D.; Cai, S. Y.; Dong, L.; Xiao, H.; Silva, S. R. P.; Liu, X. Y.; Xu, Z. X. Phthalocyanine in perovskite solar cells: a review. *Mater. Chem. Front* **2023**, *7* (9), 1704–1736.
- (30) Lu, H.; Kobayashi, N. Optically Active Porphyrin and Phthalocyanine Systems. *Chem. Rev.* **2016**, *116* (10), 6184–6261.
- (31) Feng, Q.; Sun, Y. W.; Gu, X.; Dong, Z. Z. Advances of Cobalt Phthalocyanine in Electrocatalytic CO2 Reduction to CO: a Mini Review. *Electrocatalysis-Us* **2022**, *13* (6), 675–690.
- (32) Jiang, J.; Bekaroğlu, O. Functional phthalocyanine molecular materials; Springer, 2010.
- (33) Wu, Y.; Jiang, Z.; Lu, X.; Liang, Y.; Wang, H. Domino electroreduction of CO(2) to methanol on a molecular catalyst. *Nature* **2019**, 575 (7784), 639–642.
- (34) Wu, Y. S.; Liang, Y. Y.; Wang, H. L. Heterogeneous Molecular Catalysts of Metal Phthalocyanines for Electrochemical CO Reduction Reactions. *Acc. Chem. Res.* **2021**, *54* (16), 3149–3159.
- (35) Wu, Y. S.; Jiang, Z.; Lin, Z. C.; Liang, Y. Y.; Wang, H. L. Direct electrosynthesis of methylamine from carbon dioxide and nitrate. *Nat. Sustain* **2021**, *4* (8), 725.
- (36) Shang, B.; Rooney, C. L.; Gallagher, D. J.; Wang, B. T.; Krayev, A.; Shema, H.; Leitner, O.; Harmon, N. J.; Xiao, L. Q.; Sheehan, C. Aqueous Photoelectrochemical CO2 Reduction to CO and Methanol over a Silicon Photocathode Functionalized with a Cobalt Phthalocyanine Molecular Catalyst. *Angew. Chem. Int. Edit* **2023**, *62* (4), e202215213.
- (37) Rooney, C.; Lyons, M.; Wu, Y.; Hu, G.; Wang, M.; Choi, C.; Gao, Y.; Chang, C. W.; Brudvig, G.; Feng, Z.; et al. Active Sites of Cobalt Phthalocyanine in Electrocatalytic CO2 Reduction to Methanol. *Angew. Chem., Int. Ed. Engl.* **2024**, *63*, No. e202310623.
- (38) Li, J.; Shang, B.; Gao, Y. Z.; Cheon, S.; Rooney, C. L.; Wang, H. L. Mechanism-guided realization of selective carbon monoxide electroreduction to methanol. *Nature Synthesis* **2023**, *2*, 1194.
- (39) Gross, L.; Mohn, F.; Moll, N.; Meyer, G.; Ebel, R.; Abdel-Mageed, W. M.; Jaspars, M. Organic structure determination using atomic-resolution scanning probe microscopy. *Nat. Chem.* **2010**, 2 (10), 821–825.
- (40) Gross, L. Recent advances in submolecular resolution with scanning probe microscopy. *Nat. Chem.* **2011**, *3* (6), 493–493.

- (41) Zhang, J.; Chen, P. C.; Yuan, B. K.; Ji, W.; Cheng, Z. H.; Qiu, X. H. Real-Space Identification of Intermolecular Bonding with Atomic Force Microscopy. *Science* **2013**, 342 (6158), 611–614.
- (42) Hapala, P.; Kichin, G.; Wagner, C.; Tautz, F. S.; Temirov, R.; Jelinek, P. Mechanism of high-resolution STM/AFM imaging with functionalized tips. *Phys. Rev. B* **2014**, *90* (8), 085421.
- (43) Zhang, J. L.; Zhao, S. T.; Telychko, M.; Sun, S.; Lian, X.; Su, J.; Tadich, A.; Qi, D. C.; Zhuang, J. C.; Zheng, Y.; et al. Reversible Oxidation of Blue Phosphorus Monolayer on Au(111). *Nano Lett.* **2019**, *19* (8), 5340–5346.
- (44) Telychko, M.; Edalatmanesh, S.; Leng, K.; Abdelwahab, I.; Guo, N.; Zhang, C.; Mendieta-Moreno, J. I.; Nachtigall, M.; Li, J.; Loh, K. P.; et al. Sub-angstrom noninvasive imaging of atomic arrangement in 2D hybrid perovskites. *Sci. Adv.* **2022**, *8* (17), No. eabj0395.
- (45) Woldu, A. R.; Huang, Z. L.; Zhao, P. X.; Hu, L. S.; Astruc, D. Electrochemical CO2 reduction (CO2RR) to multi-carbon products over copper-based catalysts. *Coordin Chem. Rev.* **2022**, *454*, 214340.
- (46) Raciti, D.; Wang, C. Recent Advances in CO2 Reduction Electrocatalysis on Copper. Acs Energy Lett. 2018, 3 (7), 1545–1556.
- (47) Abdinejad, M.; Mirza, Z.; Zhang, X. A.; Kraatz, H. B. Enhanced Electrocatalytic Activity of Primary Amines for CO2 Reduction Using Copper Electrodes in Aqueous Solution. *Acs Sustain Chem. Eng.* **2020**, 8 (4), 1715.
- (48) Kuhl, K. P.; Cave, E. R.; Abram, D. N.; Jaramillo, T. F. New insights into the electrochemical reduction of carbon dioxide on metallic copper surfaces. *Energ Environ. Sci.* **2012**, *5* (5), 7050–7059.
- (49) Lu, X.; Hipps, K. W.; Wang, X. D.; Mazur, U. Scanning tunneling microscopy of metal phthalocyanines: d(7) and d(9) cases. *J. Am. Chem. Soc.* **1996**, *118* (30), 7197–7202.
- (50) Weymouth, A. J.; Riegel, E.; Simmet, B.; Gretz, O.; Giessibl, F. J. Lateral Force Microscopy Reveals the Energy Barrier of a Molecular Switch. *ACS Nano* **2021**, *15* (2), 3264–3271.
- (51) Avouris, P.; Lyo, I. W.; Walkup, R. E.; Hasegawa, Y. Real-Space Imaging of Electron-Scattering Phenomena at Metal-Surfaces. *J. Vac Sci. Technol. B* **1994**, *12* (3), 1447–1455.
- (52) Albers, B. J.; Liebmann, M.; Schwendemann, T. C.; Baykara, M. Z.; Heyde, M.; Salmeron, M.; Altman, E. I.; Schwarz, U. D. Combined low-temperature scanning tunneling/atomic force microscope for atomic resolution imaging and site-specific force spectroscopy. *Rev. Sci. Instrum.* **2008**, *79* (3), No. 033704.
- (53) Chen, P.; Fan, D.; Zhang, Y.; Selloni, A.; Carter, E. A.; Arnold, C. B.; Dankworth, D. C.; Rucker, S. P.; Chelikowsky, J. R.; Yao, N. Breaking a dative bond with mechanical forces. *Nat. Commun.* **2021**, *12* (1), 5635.
- (54) Jiang, N.; Foley, E. T.; Klingsporn, J. M.; Sonntag, M. D.; Valley, N. A.; Dieringer, J. A.; Seideman, T.; Schatz, G. C.; Hersam, M. C.; Van Duyne, R. P. Observation of multiple vibrational modes in ultrahigh vacuum tip-enhanced Raman spectroscopy combined with molecular-resolution scanning tunneling microscopy. *Nano Lett.* **2012**, *12* (10), 5061–5067.
- (55) Wang, Y. F.; Wu, K.; Kroger, J.; Berndt, R. Structures of phthalocyanine molecules on surfaces studied by STM. *Aip Adv.* **2012**, 2 (4), 041402.
- (56) Baran, J. D.; Larsson, J. A.; Woolley, R. A. J.; Cong, Y.; Moriarty, P. J.; Cafolla, A. A.; Schulte, K.; Dhanak, V. R. Theoretical and experimental comparison of SnPc, PbPc, and CoPc adsorption on Ag(111). *Phys. Rev. B* **2010**, *81* (7), 075413.
- (57) Baran, J. D.; Larsson, J. A. Theoretical Insights into Adsorption of Cobalt Phthalocyanine on Ag(111): A Combination of Chemical and van der Waals Bonding. *J. Phys. Chem. C* **2013**, *117* (45), 23887–23898.
- (58) Nguyen, D.; Kang, G.; Chiang, N. H.; Chen, X.; Seideman, T.; Hersam, M. C.; Schatz, G. C.; Van Duyne, R. P. Probing Molecular-Scale Catalytic Interactions between Oxygen and Cobalt Phthalocyanine Using Tip-Enhanced Raman Spectroscopy. *J. Am. Chem. Soc.* **2018**, *140* (18), 5948–5954.
- (59) Wang, Y.; Ge, X.; Manzano, C.; Kroger, J.; Berndt, R.; Hofer, W. A.; Tang, H.; Cerda, J. Supramolecular patterns controlled by electron interference and direct intermolecular interactions. *J. Am. Chem. Soc.* **2009**, *131* (30), 10400–10402.

- (60) Wu, R. T.; Yan, L. H.; Zhang, Y. F.; Ren, J. H.; Bao, D. L.; Zhang, H. G.; Wang, Y. L.; Du, S. X.; Huan, Q.; Gao, H. J. Self-Assembled Patterns and Young's Modulus of Single-Layer Naphthalocyanine Molecules on Ag(111). *J. Phys. Chem. C* 2015, 119 (15), 8208–8212.
- (61) Maurer, R. J.; Ruiz, V. G.; Camarillo-Cisneros, J.; Liu, W.; Ferri, N.; Reuter, K.; Tkatchenko, A. Adsorption structures and energetics of molecules on metal surfaces: Bridging experiment and theory. *Prog. Surf. Sci.* **2016**, *91* (2), 72–100.
- (62) Campbell, C. T. Energies of Adsorbed Catalytic Intermediates on Transition Metal Surfaces: Calorimetric Measurements and Benchmarks for Theory. *Acc. Chem. Res.* **2019**, *52* (4), 984–993.
- (63) Araujo, R. B.; Rodrigues, G. L. S.; dos Santos, E. C.; Pettersson, L. G. M. Adsorption energies on transition metal surfaces: towards an accurate and balanced description. *Nat. Commun.* **2022**, *13* (1), 6853. (64) Lee, H. J.; Ho, W. Single-bond formation and characterization with a scanning tunneling microscope. *Science* **1999**, 286 (5445), 1719–1722.
- (65) Bartels, L.; Meyer, G.; Rieder, K. H.; Velic, D.; Knoesel, E.; Hotzel, A.; Wolf, M.; Ertl, G. Dynamics of electron-induced manipulation of individual CO molecules on Cu(III). *Phys. Rev. Lett.* **1998**, *80* (9), 2004–2007.
- (66) Albers, B. J.; Schwendemann, T. C.; Baykara, M. Z.; Pilet, N.; Liebmann, M.; Altman, E. I.; Schwarz, U. D. Data acquisition and analysis procedures for high-resolution atomic force microscopy in three dimensions. *Nanotechnology* **2009**, *20* (26), No. 264002.
- (67) Baykara, M. Z.; Dagdeviren, O. E.; Schwendemann, T. C.; Monig, H.; Altman, E. I.; Schwarz, U. D. Probing three-dimensional surface force fields with atomic resolution: Measurement strategies, limitations, and artifact reduction. *Beilstein J. Nanotech* **2012**, *3*, 637–650
- (68) Abe, M.; Sugimoto, Y.; Custance, O.; Morita, S. Room-temperature reproducible spatial force spectroscopy using atom-tracking technique. *Appl. Phys. Lett.* **2005**, 87 (17), 173503.
- (69) Akima, H. A New Method of Interpolation and Smooth Curve Fitting Based on Local Procedures. *J. Acm* **1970**, *17* (4), 589.
- (70) Akima, H. Method of Bivariate Interpolation and Smooth Surface Fitting Based on Local Procedures. *Commun. Acm* **1974**, *17* (1), 18–20.
- (71) Giessibl, F. J. Forces and frequency shifts in atomic-resolution dynamic-force microscopy. *Phys. Rev. B* **1997**, *56* (24), 16010–16015.
- (72) Sader, J. E.; Jarvis, S. P. Accurate formulas for interaction force and energy in frequency modulation force spectroscopy. *Appl. Phys. Lett.* **2004**, *84* (10), 1801–1803.
- (73) Dagdeviren, O. E.; Zhou, C.; Altman, E. I.; Schwarz, U. D. Quantifying Tip-Sample Interactions in Vacuum Using Cantilever-Based Sensors: An Analysis. *Phys. Rev. Appl.* **2018**, 9 (4), 044040.
- (74) Giessibl, F. J. High-speed force sensor for force microscopy and profilometry utilizing a quartz tuning fork. *Appl. Phys. Lett.* **1998**, 73 (26), 3956–3958.
- (75) Dagdeviren, O. E.; Schwarz, U. D. Optimizing qPlus sensor assemblies for simultaneous scanning tunneling and noncontact atomic force microscopy operation based on finite element method analysis. *Beilstein J. Nanotech* **2017**, *8*, 657–666.
- (76) Neu, M.; Moll, N.; Gross, L.; Meyer, G.; Giessibl, F. J.; Repp, J. Image correction for atomic force microscopy images with functionalized tips. *Phys. Rev. B* **2014**, *89* (20), 205407.
- (77) Sun, Z.; Boneschanscher, M. P.; Swart, I.; Vanmaekelbergh, D.; Liljeroth, P. Quantitative atomic force microscopy with carbon monoxide terminated tips. *Phys. Rev. Lett.* **2011**, *106* (4), No. 046104.
- (78) Weymouth, A. J.; Hofmann, T.; Giessibl, F. J. Quantifying molecular stiffness and interaction with lateral force microscopy. *Science* **2014**, 343 (6175), 1120–1122.
- (79) Jelinek, P. High resolution SPM imaging of organic molecules with functionalized tips. *J. Phys-Condens Mat* **2017**, 29 (34), 343002.
- (80) Lennard-Jones, J. E. Cohesion. P Phys. Soc. 1931, 43, 461-482.
- (81) Eisenschitz, R.; London, F. Über das Verhältnis der van der Waalsschen Kräfte zu den homöopolaren Bindungskräften. Zeitschrift für Physik 1930, 60 (7), 491–527.
- (82) Guggisberg, M.; Bammerlin, M.; Loppacher, C.; Pfeiffer, O.; Abdurixit, A.; Barwich, V.; Bennewitz, R.; Baratoff, A.; Meyer, E.;

- Guntherodt, H. J. Separation of interactions by noncontact force microscopy. *Phys. Rev. B* **2000**, *61* (16), 11151–11155.
- (83) Frenkel, D.; Smit, B. Understanding molecular simulation: from algorithms to applications; Academic Press, 2023.
- (84) Ellner, M.; Pavlicek, N.; Pou, P.; Schuler, B.; Moll, N.; Meyer, G.; Gross, L.; Peréz, R. The Electric Field of CO Tips and Its Relevance for Atomic Force Microscopy. *Nano Lett.* **2016**, *16* (3), 1974–1980.
- (85) Liebig, A.; Hapala, P.; Weymouth, A. J.; Giessibl, F. J. Quantifying the evolution of atomic interaction of a complex surface with a functionalized atomic force microscopy tip. *Sci. Rep-Uk* **2020**, *10* (1), 14104.
- (86) Batsanov, S. S. Van der Waals radii of elements. *Inorg. Mater*+2001, 37 (9), 871–885.
- (87) Badenhoop, J. K.; Weinhold, F. Natural steric analysis: Ab initio van der Waals radii of atoms and ions. *J. Chem. Phys.* **1997**, *107* (14), 5422–5432.
- (88) Wu, W.; Harrison, N. M.; Fisher, A. J. Electronic structure and exchange interactions in cobalt-phthalocyanine chains. *Phys. Rev. B* **2013**, 88 (2), 024426.
- (89) Zhou, Q. F.; Liu, Z. F.; Marks, T. J.; Darancet, P. Electronic Structure of Metallophthalocyanines, MPc (M = Fe, Co, Ni, Cu, Zn, Mg) and Fluorinated MPc. *J. Phys. Chem. A* **2021**, *125* (19), 4055–4061.
- (90) Zhao, A. D.; Li, Q. X.; Chen, L.; Xiang, H. J.; Wang, W. H.; Pan, S.; Wang, B.; Xiao, X. D.; Yang, J. L.; Hou, J. G.; et al. Controlling the Kondo effect of an adsorbed magnetic ion through its chemical bonding. *Science* **2005**, *309* (5740), 1542–1544.
- (91) Mönig, H. Copper-oxide tip functionalization for submolecular atomic force microscopy. *Chem. Commun.* **2018**, *54* (71), 9874–9888.
- (92) Zahl, P.; Bierkandt, M.; Schroder, S.; Klust, A. The flexible and modern open source scanning probe microscopy software package GXSM. *Rev. Sci. Instrum.* **2003**, 74 (3), 1222–1227.
- (93) Zahl, P.; Wagner, T.; Moller, R.; Klust, A. Open source scanning probe microscopy control software package GXSM. *J. Vac Sci. Technol. B* **2010**, 28 (3), C4E39.
- (94) Zahl, P.; Wagner, T. GXSM Smart & Customizable SPM Control. *Imaging & Microscopy* **2015**, No. 1, 38.
- (95) Dagdeviren, O. E.; Schwarz, U. D. Numerical performance analysis of quartz tuning fork-based force sensors. *Meas Sci. Technol.* **2017**, 28 (1), 015102.
- (96) Drakova, D.; Nedjalkova, M.; Doyen, G. Theory of tip-dependent Imaging of adsorbates in the STM: CO on Cu(111). *Int. J. Quantum Chem.* **2006**, *106* (6), 1419–1431.
- (97) Hansen, W.; Bertolo, M.; Jacobi, K. Physisorption of Co on Ag(111) Investigation of the Monolayer and the Multilayer through Hreels, Arups, and Tds. *Surf. Sci.* **1991**, 253 (1–3), 1–12.